Key Points:
- t* spectral decay method was used to obtain attenuation structure beneath Sierra Negra
- High-attenuation anomaly from 0.5 to 10.5 km depth interpreted as possible magma accumulation zones
- Results support a shallow magma body described and modeled in caldera deformation studies

Three-dimensional attenuation model of Sierra Negra Volcano, Galápagos Archipelago

Rebecca L. Rodd[1], Jonathan M. Lees[1], and Gabrielle Tepp[2]

[1]Department of Geological Sciences, University of North Carolina at Chapel Hill, Chapel Hill, North Carolina, USA,
[2]Department of Physics and Astronomy, University of Rochester, Rochester, New York, USA

Abstract The shallow magma system beneath Sierra Negra was imaged using attenuation tomographic methods. The t^* spectral decay method for P wave phases was used to highlight regions of high Q_p^{-1} which suggest the presence of magma melt. High-Q_p^{-1} anomalies ranging from 0.005 to 0.04 are concentrated below the caldera from 0.5 to 10.5 km depths. Attenuation is sensitive to temperature and fluid presence; thus, this high attenuation is interpreted as possible zones of magma accumulation. An imaged shallow body is consistent with geodetic studies on caldera deformation that modeled a magma sill or flattopped diapir of unknown thickness at ∼1 km depth below sea level.

1. Introduction

Sierra Negra is one of the most active volcanoes in the Galápagos Archipelago. It has a shallow, elliptical caldera (7×10 km) and a sinuous ridge formed from near-vertical faults that run roughly parallel to the eastern and southern caldera [*Reynolds et al.*, 1995; *Jonsson et al.*, 2005]. On average, eruptions occur every 15 years and produce $1 \cdot 10^6$ m³/yr basalt deposits [*Reynolds et al.*, 1995]. Petrologic evidence suggests that magma ponding occurs from 4 to 11 km replenished by a partially melted garnet source [*Reynolds and Geist*, 1995]. Deformation modeling indicates that episodic intrusions from a deep source pressurizes a flattopped magma sill or diapir at ∼1 km below sea level causing domed inflation, trapdoor faulting, and often magma extrusion [*Amelung et al.*, 2000; *Jonsson et al.*, 2005; *Yun et al.*, 2006; *Chadwick et al.*, 2006; *Geist et al.*, 2008]. Ongoing inflation in conjunction with high caldera seismicity indicates that the shallow magma reservoir and deeper source are persistent features. Despite the reservoir's control on deformation, faulting, and eruptive behavior, the shallow reservoir had not been imaged seismically prior to this study.

Body wave tomography identified a patchwork of high- and low-V_p anomalies beneath southern Isabela Island [*Tepp et al.*, 2014]. The results indicate a large low-V_p zone with volumetrically smaller, lower V_p anomalies within the larger body. This body is interpreted as a large crystal mush zone with low-percent melt beneath and north of the caldera from 5.5 to 15 km depth. The V_p model was unable to image the shallow structure < 3 km or to constrain any smaller bodies of high-percent melt that exist within the broader low-V_p zone. Other studies focus on deeper structures, such as the mantle plume and impedance boundaries beneath Galápagos [*Villagomez et al.*, 2007; *Gibson and Geist*, 2010; *Rychert et al.*, 2014; *Villagomez et al.*, 2014].

In this study, attenuation tomography is used to better define the shallow magma system beneath Sierra Negra's caldera. Seismic attenuation is strongly dependent on temperature and fluid content [*Kampfmann and Berckhemer*, 1985; *Jackson*, 1993] and is particularly useful in studying volcanic media where attenuation is closely linked to the thermal state (e.g., magma accumulation, partial melt) and volcanic subsurface structure (e.g., heterogeneities due to volcanoclastic deposit). The attenuation structure beneath Sierra Negra is imaged with the spectral decay method. Despite difficulties in modeling and high scatter, this method has successfully imaged attenuation structures in various volcanic media [e.g., *De Siena et al.*, 2009, 2010; *Koulakov et al.*, 2014; *Ohlendorf et al.*, 2014, *Lin et al.*, 2015]. We interpret our Q_p^{-1} model in context of current V_p [*Tepp et al.*, 2014] and models of surface deformation [*Amelung et al.*, 2000; *Yun et al.*, 2006].

2. Data

We analyzed data from the 15 broadband seismic stations in the SIGNET array deployed on Isabela Island from July 2009 to June 2011 shown in Figure 1 [*Tepp et al.*, 2014]. Earthquakes were located with Rquake [*Lees*, 2015]
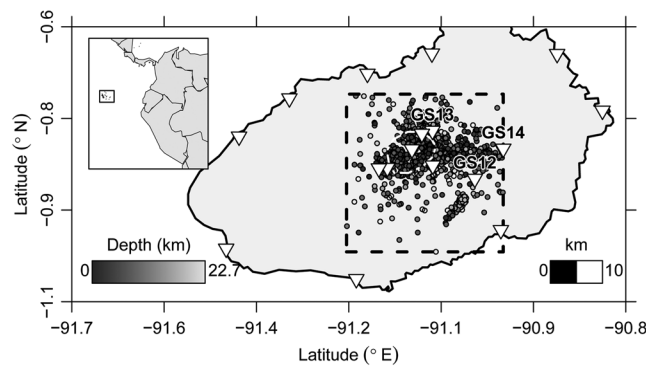
Figure 1. Map of southern Isabella Island and Sierra Negra caldera (white dashed ellipse) with SIGNET array stations shown in light gray triangles. Black dashed rectangle outlines the grid boundaries and the region in which earthquakes and stations were limited. Earthquakes included in the inversion are shown as large circles colored by depth. Stations GS12, GS13, and GS14 are labeled and correspond to the seismograms and spectra shown in Figure 2. The other stations located within the grid boundaries are used in the inversion but are not labeled. Inset map in top left corner displays the Galápagos Archipelago relative to South America.

using manually picked *P* and *S* wave phase arrivals. A 30 × 30 km grid with 0.5 km spacing was selected for the inversion (black dashed rectangle in Figure 1). Only the 8 stations and 309 of 1737 earthquakes within the grid were used. Poorly located earthquakes and earthquakes located outside of the grid were excluded.

3. Methods

3.1. t^* Spectral Decay

The 3-D attenuation structure was determined using the spectral decay method in which the attenuation operator, t^*, was estimated for each raypath by modeling the amplitude spectrum of earthquake ground displacement. The observed spectrum is a convolution of the earthquake source, path effects, instrument response, and site response

as described by *Scherbaum* [1990]. Instrument response was removed prior to computing the amplitude displacement spectra. Unusual variations observed in spectra for a single station and/or nearby stations would suggest a local site response. Often this variation is observed as a bump in the amplitude spectra [*Bennington et al.*, 2008]. This behavior was not observed in the data; thus, site response was not included in the spectral inversion.

The amplitude spectra were modeled as

$$A(f) = \frac{\Omega_0 e^{-\pi f t^*}}{\left(1 + \left(\frac{f}{f_c}\right)^{n\gamma}\right)^{1/n}} \quad (1)$$

$$t^* = t_0^* f^{-\alpha} \quad (2)$$

where f is the frequency, t^* is the attenuation operator, α is the frequency dependence of attenuation, f_c is the source corner frequency, Ω_0 is the low-frequency plateau amplitude, and γ is the falloff of the displacement spectra above f_c. When $\gamma = 2$ and $n = 1$, the model is equivalent to the f^2 Brune source model [*Brune*, 1970]. This model is assumed for several earthquake source studies [e.g., *Randall*, 1973] and spectral decay attenuation tomography [e.g., *Scherbaum*, 1990; *Rietbrock*, 2001; *Eberhart-Phillips and Chadwick*, 2002]. We assumed a modification of the f^2 model with $n = 2$ [*Boatwright*, 1978; *Abercrombie*, 1995; *Lindley and Archuleta*, 1992] which produces a sharper corner and better fits the spectra.

3.2. Spectral Modeling

Amplitude spectra were determined using the multitaper method for a 1 s time window around the *P* wave arrival [*Lees and Park*, 1995]. Waveforms with a *P-S* arrival time difference <1 s were excluded to avoid contamination from *S* wave energy. A noise spectrum was calculated from a 1 s time window selected prior to the arrival. In order to ensure quality t^* values, only spectra with SNR > 2.5 across a continuous frequency band from 2 to 15 Hz were included.

The amplitude source spectra were modeled using equation (1). It is not possible to obtain a unique best fit solution with the five free parameters: γ, α, t^*, f_c, and Ω_0. Therefore, γ and α were fixed, while initially, f_c, t^*, and Ω_0 were allowed to vary. This study corroborates previous findings that $\gamma = 2$ provides the best fit results [e.g., *Boatwright*, 1978; *Scherbaum*, 1990; *Lindley and Archuleta*, 1992; *Abercrombie*, 1995; *Eberhart-Phillips and Chadwick*, 2002].
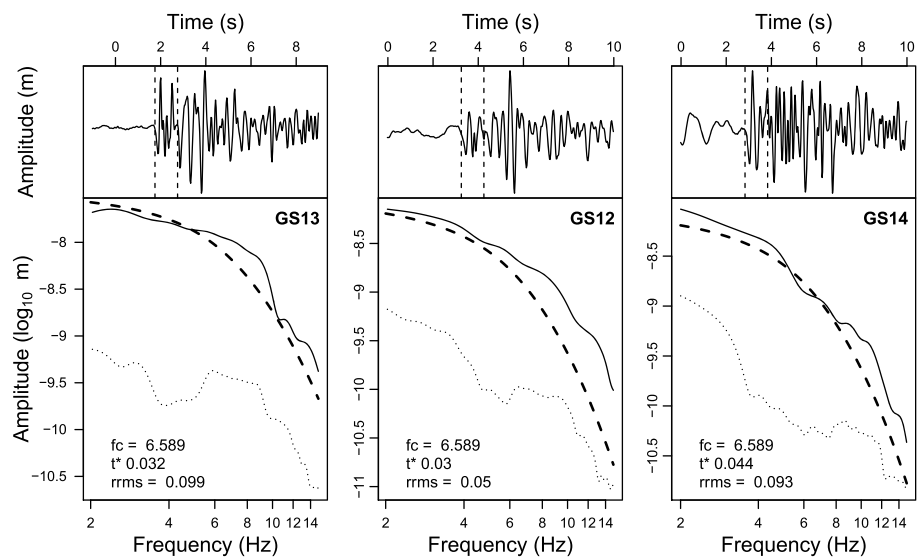
Although laboratory studies determined that seismic attenuation is a frequency-dependent process which could affect t^* results [*Bellis and Holtzman*, 2014], tomography studies have conflicting results for α. Previous studies suggested that $-1 < \alpha < 0$ provides the best fit to the amplitude spectra [*Hough et al.*, 1999;

Figure 2. Examples of *P* wave seismograms and spectra of the same earthquake recorded at stations GS13, GS12, and GS14. This earthquake occurred on 11 December 2009 just north of GS13. The dashed lines on the seismograms indicate the selection window for the computation of the fast Fourier transform. *P* wave spectra, spectral fits, and noise spectra are shown by solid, dashed, and dotted lines, respectively. t^*, f_c, and residual RMS are shown in the bottom left corner of each spectra plot.

Lindley and Archuleta, 1992; *Sarker and Abers*, 1998]. Other studies found that frequency-independent *Q* produces the best fit or an equivalent fit to frequency-dependent *Q*, in which case frequency-independent *Q* is assumed for model simplicity [*Scherbaum*, 1990; *Lees and Lindley*, 1994; *Rietbrock*, 2001; *De Lorenzo et al.*, 2010]. Due to these varying results, spectral modeling was repeated several times with α set to fixed values between −1 and 1. Although attenuation results were similar for all α, resolution and recovery varied significantly due to discrepancies in the amount of usable t^* values. When $\alpha = -0.2$, the mean residual RMS is minimized and number of usable t^* is maximized. Therefore, $\alpha = -0.2$ was used for the final inversion.

The Levenberg-Marquardt method was used to model the amplitude spectra. Initially, t^*, f_c, and Ω_0 were allowed to vary freely, but models showing extreme f_c outliers were removed. When t^* and f_c are allowed to vary freely, there is often a trade-off between the two parameters [*Lees and Lindley*, 1994]. Given f_c is a source parameter, f_c should be the same for all raypaths from a single event. Initial modeling resulted in large fluctuations in f_c for all raypaths, with f_c ranging from 2 to 15 Hz (Figure S1 in the supporting information). Thus, we repeated the modeling with f_c constrained to the mean f_c for all raypaths of an event. The mean f_c was iteratively solved by limiting f_c to within the mean ±1 standard deviation of the previous f_c until convergence to a single solution. This modeling reduced the large fluctuations in f_c (Figure S2). An example of the amplitude spectrum and modeling results are depicted in Figure 2. The t^* values obtained from the final modeling with average f_c were used for the attenuation inversion.

3.3. Q_p^{-1} Inversion

The attenuation, Q^{-1}, can be determined from t^* using

$$t^* = \int_{\text{raypath}} Q^{-1}(x, y, z) \cdot \frac{1}{v(x, y, z)} \cdot dr(x, y, z) \tag{3}$$

where $v(x, y, z)$ is the 3-D velocity model. Equation (3) was used to obtain a Q^{-1} model of *P* wave phases (Q_p^{-1}) for each α. The line integral was discretized into 0.5×0.5 km blocks at 0, 0.5, 3, 5.5, 8, 10.5, and 13 km depths with respect to sea level where the attenuation is assumed constant in each block.

A 3-D velocity model already exists for V_p, so we chose to use this model for $v(x, y, z)$ in our inversion. In our region of study, the V_p model is well resolved below 3 km depth and has good resolution for small bodies (~2.5 km dimensions) at 0.5–3 km [*Tepp et al.*, 2014]. This model used larger grid spacing which needed to be interpolated. The interpolation could introduce uncertainty, so we tested various interpolations as well as newly derived models based on the limited raypaths in the smaller grid region. The minor differences in
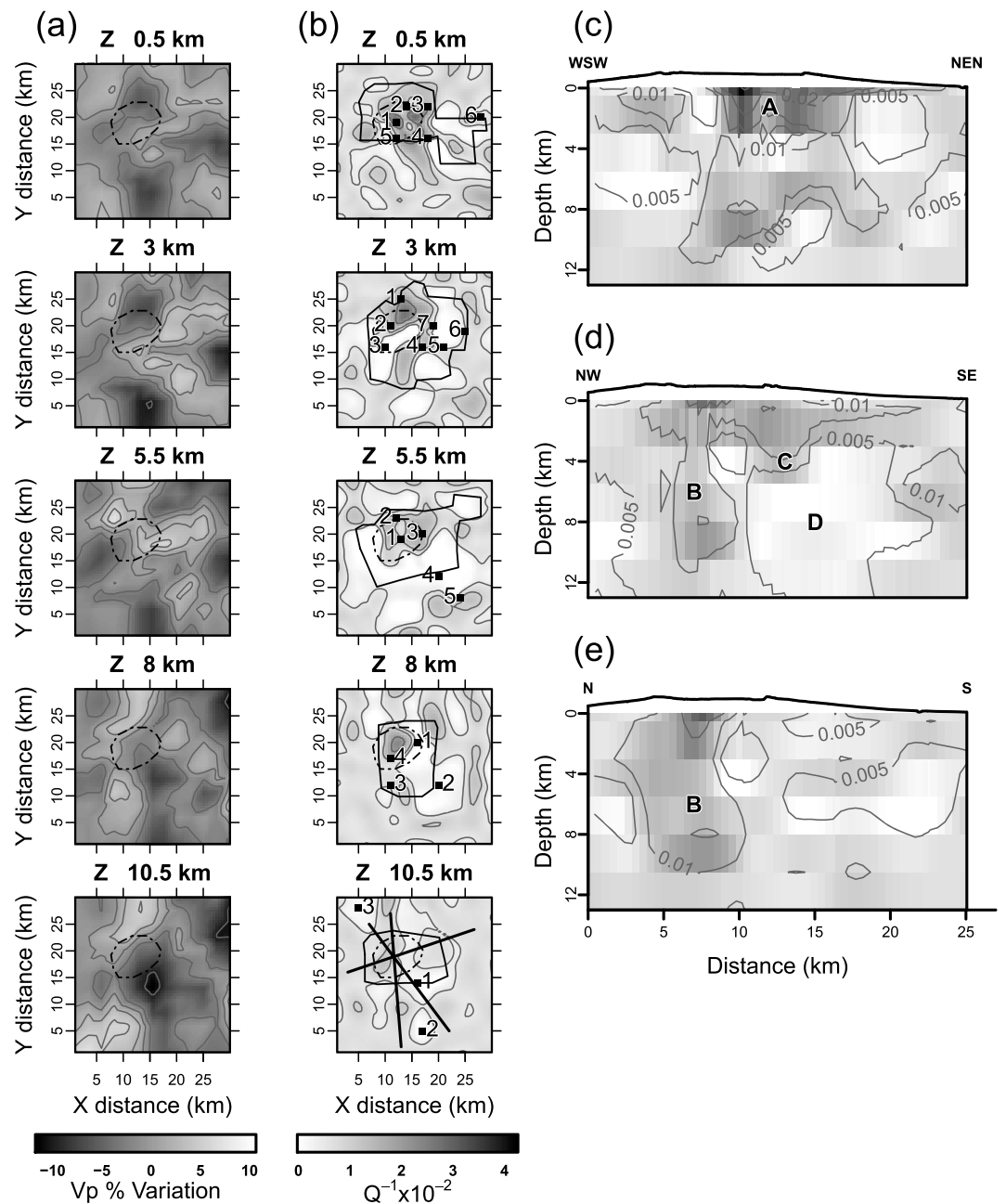
Figure 3. Model of (a) interpolated V_p derived from body wave tomography [*Tepp et al.*, 2014] and (b) Q_p^{-1} shown in five panels corresponding to varying depth layers. Points labeled by numbers in (Figure 3b) correspond to spike test points in Table S1. Thick black solid lines in Figure 3b (fifth panel) correspond to the (c–e) vertical cross sections. Resolvable regions are outlined by thin black polygons where regions outside the polygons are not resolvable. Contours correspond to Q_p^{-1} of 0.005, 0.01, 0.02, and 0.04.

these velocity models did not significantly affect Q_p^{-1}; thus, the V_p model from *Tepp et al.* [2014] interpolated to 0.5 km spacing was used for the final inversion (Figure 3a).

In the inversion, raypaths were weighted by SNR and t^* residual RMS. t^* were averaged for rays that follow the same path so that clusters of earthquakes did not bias the inversion result. A 2-D Laplacian regularization multiplied by a damping parameter was applied to minimize curvature between nearby blocks and overcome noise levels. Several damping parameters were tested to find the minimization of residual norm and model length. The optimal damping parameter, 0.75, was determined using the trade-off curve between model

length and residual norm (Figure S3). Following a similar approach as *Lin et al.* [2015], a background $Q_p^{-1} = 0.0067$ minimized residuals after a single iteration and was used as the background model for the final inversion. LSQR was used to solve this inversion problem to obtain the Q_p^{-1} perturbations [*Paige and Saunders*, 1982]. Negative Q_p^{-1} values were not allowed since negative attenuation is physically unrealistic. This a priori constraint was included in the iteration algorithm in LSQR [see *Herman*, 1980].

4. Synthetic Data Testing

Spike and checkerboard tests were used to ascertain the resolution and smearing of the model. For the spike test, a $Q_p^{-1} = 0.03$ perturbation is added to a single block (i.e., grid point) in a homogeneous near-zero background attenuation. Synthetic t^* for all raypaths is computed through the perturbed model and inverted to recover the perturbed spike. Spike tests were calculated and used to estimate resolution at various key points in the model (points labeled by numbers in Figure 3b). Results indicate that resolution is best within the caldera and the nearby surrounding region. Outside the caldera, resolution has large fluctuations, ranging from 1 to 10 km in size (Table S1).

Several checkerboard patterns with varying dimensions of high (~ 0.05) and low perturbations (~ 0.001) were created. Synthetic t^* was computed through the perturbed models and inverted to solve Q_p^{-1} (Figures S4–S6). A second set of checkerboard tests were run with random noise added to the synthetic data prior to the inversion (Figure S7). Addition of noise does not significantly affect the recovered checkerboard pattern, but recovery of the perturbed Q_p^{-1} magnitudes is reduced at deeper depths. Fine-scale (3 km) (Figure S4) and large-scale (6 km) (Figure S5) checkers are resolvable beneath and east of the caldera from 0.5 to 8 km depths, although recovery of the magnitudes of Q_p^{-1} is poorer at 8 km depth. Despite poor resolution and significant smearing, there are high- and low-attenuation checkers present from 8 to 10.5 km depth. Depths >10.5 km are not resolvable and are not included in the results. The minimum resolvable structure in the study region is 2.5 km, which is similar to the resolution of the V_p model in our study region [*Tepp et al.*, 2014].

5. Results

Results from the final tomographic inversion is plotted in five panels corresponding to different depth layers in Figure 3b. The V_p model [*Tepp et al.*, 2014] is presented beside the attenuation results for comparison. Only anomalies in areas of good resolution (outlined by a thin line in Figure 3b) are described.

High attenuation is concentrated beneath the caldera from 0 to 10.5 km depth. This zone is partially continuous, although there are significant spatial and magnitude variations in Q_p^{-1}. From 0 to 3 km depth, there is high attenuation ranging from 0.01 to 0.04, directly beneath the caldera (Anomaly A) which correlates with low V_p [*Tepp et al.*, 2014]. The top of Anomaly A extends northeast and southeast of the caldera rim. Accounting for poor resolution and smearing, the diameter extends ~ 2 km beyond the caldera rim. Additionally, west of the caldera, there is a small high-attenuation ($Q_p^{-1} \sim 0.01$) circular zone. From 3 to 5.5 km depth, high attenuation ($Q_p^{-1} \sim 0.02$) is concentrated under the northern caldera (Anomaly B). At 3 km, there is a low-V_p anomaly, but it is further north than Anomaly B. There is a high-attenuation cylindrical zone with $Q_p^{-1} \sim 0.005$ under the southern caldera at this depth as well (Anomaly C). It is evident in cross section that Anomaly B deepens southward and decreases in magnitude from 5.5 to 10.5 km depth (Figures 3c–3e).

Low-attenuation anomalies (Anomaly D) surround the high-attenuation zones. From 3 to 5.5 km depth, Anomaly D is concentrated under the eastern region. From 5.5 to 8 km depth, Anomaly D is present under the eastern, southern, and western caldera. At 8 km depth, low attenuation is primarily concentrated in the southeastern area. There are no significant attenuation anomalies below 10.5 km depth though resolution is too poor to rule out any such anomalies.

6. Model Uncertainty

6.1. Variance of Q_p^{-1}

A jackknife statistical test was used to estimate the variance for each block of the Q_p^{-1} model following a similar approach as *Lees and Lindley* [1994] (Figure S8). Variances range from 0 to 0.008. In blocks with zero coverage, the variance is zero. The mean variance, excluding blocks with zero coverage, is 0.0005. This is low relative to the values from the resolved Q_p^{-1} model. Blocks with good coverage have the smallest uncertainty. At depths

<0.5 km, the largest uncertainty is concentrated beneath stations where raypaths converge. Other large uncertainties are concentrated in regions with low coverage and/or near blocks with zero coverage.

6.2. Probability of Randomness

In high-scattering regimes, loss of $t*$ signal coherence can occur [*De Siena et al.*, 2010]. Volcanic cones tend to be highly heterogeneous resulting in a high-scattering regime. Therefore, loss of signal coherence is a concern in the study area. If signal coherence is lost, $t*$ determinations will not be spatially correlated and will appear random. The probability that the observed Q_p^{-1} model parameters are a result of random $t*$ was calculated using Monte Carlo simulations. Synthetic random data sets of length, mean, and standard deviation equal to the observed $t*$ were inverted to produce 10,000 synthetic models. For each block, the number of synthetic Q_p^{-1} values that lie between the observed $Q_p^{-1} \pm$ variance is divided by the number of simulations to determine the probability of randomness (Figure S9). Blocks with zero coverage have 0% randomness since the variance is also zero. Above 0.5 km, randomness is large especially beneath the caldera which suggests loss of signal coherence due to a high-scattering regime. Thus, depths <0.5 km are not interpreted. There are regions of large randomness from 3 to 5.5 km depths outside the caldera that are associated with low ray coverage. Randomness is low below the caldera at depths > 0.5 km. Therefore, the observed Q_p^{-1} are likely to be real features of the path effects.

7. Discussion

High Q_p^{-1} is most commonly attributed to magma accumulation, temperature gradients, fluid presence, magma movement, and heterogeneous media in volcanic settings [*Lees*, 2007]. Q_p^{-1} should be studied in conjunction with V_p, V_s, V_p/V_s, Q_s^{-1}, and the scattering coefficient, g, to differentiate the causes of attenuation. Since only the V_p model is well resolved, our interpretation of the attenuation structure and understanding of the magmatic system is limited. Only areas that are well resolved by the velocity [*Tepp et al.*, 2014] and attenuation analyses are interpreted.

High attenuation is present below the caldera from 0.5 to 10.5 km depth. The magnitude of this high attenuation tends to decrease with depth until 10.5 km where resolution is poor. This trend is expected due to increased confining pressure. Poorer magnitude recovery at depths > 5.5 km could also produce this trend (Table S1 and Figures S4–S7).

The high-attenuation region is divided into three anomalies. The relative uniformity in Q_p^{-1} between Anomaly B and Anomaly C suggests that the rock properties and thermal state of the system are similar in these two regions. However, Anomaly A is spatially separated and varies in Q_p^{-1} magnitude from Anomalies B and C, suggesting it is a separate attenuating body.

Given that attenuation is sensitive to temperature [e.g., *Kampfmann and Berckhemer*, 1985; *Jackson and Faul*, 2010], it is likely that high temperatures contribute to the high-attenuation anomalies. However, the studies on sensitivity to temperature are based on mantle compositions; thus, a temperature estimate cannot be derived for this region. Correlations between V_s and Q^{-1} in tomography studies suggest Q^{-1} is also dependent on melt percent, although this is not yet quantified [*Hammond and Humphreys*, 2000]. There is a significant low-U_g signature for 2 s and 3 s periods derived from ambient noise tomography (K. Seats, personal communication, 2015) which could translate to low V_s at shallow depths. Based on the Q_p^{-1} and V_p results, we can only speculate that partial melting may contribute to the observed high-attenuation signals. Given the sensitivities to temperature and melt, we interpret the high-attenuation anomalies as possible zones of magma accumulation beneath the caldera.

The low-attenuation anomaly, Anomaly D, roughly correlates with a high-V_p anomaly from 3 to 5.5 km depth. In volcanic settings, low Q_p^{-1} and high V_p are most commonly attributed to cooled mafic compositions with limited fluid presence [*Lees*, 2007]. From 5.5 to 8 km, low-Q_p^{-1} anomalies correspond to low V_p which is atypical. *Lin et al.* [2015] observed similar low-Q_p^{-1} values with low V_p and low V_p/V_s and attributed this to melt-saturated rock. Without a V_p/V_s ratio, we interpret the low Q_p^{-1} anomalies as shallow cumulate mafic rock on the edges of deeper magma accumulation.

7.1. Comparison to Current Magma System Models

If Anomalies A and B are considered two different zones of magma accumulation, this would suggest at least two stacked reservoirs: one shallow body between 0.5 and 3 km depth controlling surface deformation and a deeper, connected zone from 3 to 10.5 km depth. The top of Anomaly A is consistent with the ~1 km depth of

the shallow magma body inferred from deformation modeling [*Amelung et al.*, 2000; *Geist et al.*, 2006; *Yun et al.*, 2006]. This shallow body is thought to be a sill that is diapiric in shape [*Chadwick and Dieterick*, 1995; *Yun et al.*, 2006]. However, distinguishing between two separate attenuating bodies is difficult due to spatial overlap and similar Q_p^{-1} signatures. Finer vertical grid spacing is required to confirm a multiple chamber geometry. Thus, it is also possible that there is a continuous magma accumulation zone with local Q_p^{-1} variations beneath Sierra Negra.

Our results provide critical detail to the results of *Tepp et al.* [2014]. Body wave tomography imaged a large low-V_p zone from 5.5 to 15 km interpreted as a large mush zone [*Tepp et al.*, 2014; *Geist et al.*, 2014]. The V_p model also suggested small, higher-melt pockets within the mush zone. We suggest that the high-attenuation anomalies correspond to these pockets within the large mush zone which is too broad to distinguish from the background in this study. Attenuation is more sensitive to temperature gradients and melt than velocity; thus, it is better able to define these high-melt pockets. Other studies have shown similar discrepancies in size of high-Q_p^{-1} and low-V_p anomalies [e.g., *Prudencio et al.*, 2015].

8. Conclusions

The spectral decay method was used to determine the Q_p^{-1} structure beneath Sierra Negra. High attenuation is concentrated primarily below the caldera from 0.5 to 10.5 km depth. From 0.5 to 3 km, the high-attenuation anomaly is heterogeneous. From 3 to 8 km, there is an elliptical high-attenuation anomaly below the caldera that deepens southward. The high-attenuation anomalies are interpreted as zones of magma accumulation. Our results support a multichamber magma system with a shallow body at ∼1 km and a deeper body at 3–10.5 km depth within the region of a larger mush zone imaged in the V_p model. Future studies modeling V_s, Q_s^{-1}, and the scattering coefficient could better distinguish the sources of high attenuation and further our understanding of the shallow magma system beneath Sierra Negra.

References

Abercrombie, R. (1995), Earthquake source scaling relationships from −1 to 5 M(L) using seismograms recorded at 2.5-km depth, *J. Geophys. Res.*, *100*(B12), 24,015–24,036, doi:10.1029/95JB02397.

Amelung, F., S. Jonsson, H. Zebker, and P. Segall (2000), Widespread uplift and 'trapdoor' faulting on Galápagos volcanoes observed with radar interferometry, *Nature*, *407*(6807), 993–996.

Bellis, C., and B. Holtzman (2014), Sensitivity of seismic measurements to frequency-dependent attenuation and upper mantle structure: An initial approach, *J. Geophys. Res. Solid Earth*, *119*, 5497–5517, doi:10.1002/2013JB010831.

Bennington, N., C. Thurber, and S. Roecker (2008), Three-dimensional seismic attenuation structure around the SAFOD site, Parkfield, California, *Bull. Seismol. Soc. Am.*, *98*(6), 2934–2947, doi:10.1785/0120080175.

Boatwright, J. (1978), Detailed spectral analysis of 2 small New-York-State earthquakes, *Bull. Seismol. Soc. Am.*, *68*(4), 1117–1131.

Brune, J. (1970), Tectonic stress and spectra of seismic shear waves from earthquakes, *J. Geophys. Res.*, *75*(26), 4997–5009, doi:10.1029/JB075i026p04997.

Chadwick, W., and J. Dieterick (1995), Mechanical modeling of circumferential and radial dike intrusion on Galápagos volcanoes, *J. Volcanol. Geotherm. Res.*, *66*(1–4), 37–52, doi:10.1016/0377-0273(94)00060-T.

Chadwick, W. W., Jr., D. J. Geist, S. Jonsson, M. Poland, D. J. Johnson, and C. M. Meertens (2006), A volcano bursting at the seams: Inflation, faulting, and eruption at Sierra Negra volcano, Galápagos, *Geology*, *34*(12), 1025–1028, doi:10.1130/G22826A.1.

De Lorenzo, S., A. Zollo, and G. Zito (2010), Source, attenuation, and site parameters of the 1997 Umbria-Marche seismic sequence from the inversion of P wave spectra: A comparison between constant $Q(P)$ and frequency-dependent $Q(P)$ models, *J. Geophys. Res.*, *115*, B09306, doi:10.1029/2009JB007004.

De Siena, L., E. Del Pezzo, F. Bianco, and A. Tramelli (2009), Multiple resolution seismic attenuation imaging at Mt. Vesuvius, *Phys. Earth Planet. Inter.*, *173*(1–2), 17–32, doi:10.1016/j.pepi.2008.10.015.

De Siena, L., E. Del Pezzo, and F. Bianco (2010), Seismic attenuation imaging of Campi Flegrei: Evidence of gas reservoirs, hydrothermal basins, and feeding systems, *J. Geophys. Res.*, *115*, B09312, doi:10.1029/2009JB006938.

Eberhart-Phillips, D., and M. Chadwick (2002), Three-dimensional attenuation model of the shallow Hikurangi subduction zone in the Raukumara Peninsula, New Zealand, *J. Geophys. Res.*, *107*(B2), 2033, doi:10.1029/2000JB000046.

Geist, D., W. Chadwick, and D. Johnson (2006), Results from new {GPS} and gravity monitoring networks at Fernandina and Sierra Negra volcanoes, Galápagos, 2000–2002, *J. Volcanol. Geotherm. Res.*, *150*(1–3), 79–97, doi:10.1016/j.jvolgeores.2005.07.003.

Geist, D., B. A. Diefenbach, D. J. Fornari, M. D. Kurz, K. Harpp, and J. Blusztajn (2008), Construction of the Galápagos platform by large submarine volcanic terraces, *Geochem. Geophys. Geosyst.*, *9*, Q03015, doi:10.1029/2007GC001795.

Geist, D. J., G. Bergantz, and W. W. Chadwick Jr. (2014), *Galápagos Magma Chambers in Galápagos: A Natural Laboratory for the Earth Sciences, Geophys. Monogr. Ser.*, vol. 204, edited by K. S. Harpp et al., pp. 55–69.

Gibson, S., and D. Geist (2010), Geochemical and geophysical estimates of lithospheric thickness variation beneath Galápagos, *Earth Planet. Sci. Lett.*, *300*(3–4), 275–286, doi:10.1016/j.epsl.2010.10.002.

Hammond, W., and E. Humphreys (2000), Upper mantle seismic wave attenuation: Effects of realistic partial melt distribution, *J. Geophys. Res.*, *105*(B5), 10,987–10,999, doi:10.1029/2000JB900042.

Herman, G. T. (1980), *Image Reconstruction From Projections*, pp. 193–196, Academic Press, New York-London.

Hough, S., J. Lees, and F. Monastero (1999), Attenuation and source properties at the Coso geothermal area, California, *Bull. Seismol. Soc. Am.*, *89*(6), 1606–1619.

Jackson, I. (1993), Progress in the experimental-study of seismic-wave attenuation, *Annu. Rev. Earth Planet. Sci.*, *21*, 375–406, doi:10.1146/annurev.earth.21.1.375.

Jackson, I., and U. H. Faul (2010), Grainsize-sensitive viscoelastic relaxation in olivine: Towards a robust laboratory-based model for seismological application, *Phys. Earth Planet. Inter.*, *183*(1–2), 151–163, doi:10.1016/j.pepi.2010.09.005.

Jonsson, S., H. Zebker, and F. Amelung (2005), On trapdoor faulting at Sierra Negra volcano, Galápagos, *J. Volcanol. Geotherm. Res.*, *144*(1–4), 59–71, doi:10.1016/j.jvolgeores.2004.11.029.

Kampfmann, W., and H. Berckhemer (1985), High-temperature experiments on the elastic and anelastic behavior of magmatic rocks, *Phys. Earth Planet. Inter.*, *40*(3), 223–247, doi:10.1016/0031-9201(85)90132-3.

Koulakov, I., S. El Khrepy, N. Al-Arifi, I. Sychev, and P. Kuznetsov (2014), Evidence of magma activation beneath the Harrat Lunayyir basaltic field (Saudi Arabia) from attenuation tomography, *Solid Earth*, *5*(2), 873–882, doi:10.5194/se-5-873-2014.

Lees, J., and G. Lindley (1994), 3-dimensional attenuation tomogrpahy at Loma-Prieta–Inversion of T-asterisk for Q, *J. Geophys. Res.*, *99*(B4), 6843–6863, doi:10.1029/93JB03460.

Lees, J. M. (2007), Seismic tomography of magmatic systems, *J. Volcanol. Geotherm. Res.*, *167*(1–4), 37–56, doi:10.1016/j.jvolgeores.2007.06.008.

Lees, J. M. (2015), *Rquake: Seismic Hypocenter Determination*, r package version 2.3-1.

Lees, J. M., and J. Park (1995), Multiple-taper spectral analysis: A stand-alone C-subroutine, *Comput. Geosci.*, *21*(2), 199–236, doi:10.1016/0098-3004(94)00067-5.

Lin, G., P. M. Shearer, F. Amelung, and P. G. Okubo (2015), Seismic tomography of compressional wave attenuation structure for Kilauea Volcano, Hawai'i, *J. Geophys. Res. Solid Earth*, *120*, 2510–2524, doi:10.1002/2014JB011594.

Lindley, G., and R. Archuleta (1992), Earthquake source parameters and the frequency-dependence of attenuation at Coalinga, Mammoth Lakes, and the Santa-Cruz Mountains, California, *J. Geophys. Res.*, *97*(B10), 14,137–14,154, doi:10.1029/92JB00550.

Ohlendorf, S. J., C. H. Thurber, J. D. Pesicek, and S. G. Prejean (2014), Seismicity and seismic structure at Okmok Volcano, Alaska, *J. Volcanol. Geotherm. Res.*, *278*, 103–119, doi:10.1016/j.jvolgeores.2014.04.002.

Paige, C., and M. Saunders (1982), LSQR—An algorithm for sparse linear-equations and sparse least-squares, *ACM Trans. Math. Softw.*, *8*(1), 43–71, doi:10.1145/355984.355989.

Prudencio, J., L. De Siena, J. M. Ibanez, E. Del Pezzo, A. Garcia-Yeguas, and A. Diaz-Moreno (2015), The 3D attenuation structure of deception Island (Antarctica), *Surv. Geophys.*, *36*(3), 371–390, doi:10.1007/s10712-015-9322-6.

Randall, M. (1973), Spectral theory of seismic sources, *Bull. Seismol. Soc. Am.*, *63*(3), 1133–1144.

Reynolds, R., and D. Geist (1995), Petrology of lavas from Sierra Negra volcano, Isabela Island, Galápagos archipelago, *J. Geophys. Res.*, *100*(B12), 24,537–24,553, doi:10.1029/95JB02809.

Reynolds, R., D. Geist, and M. Kurz (1995), Physical volcanology and structural development of Sierra Negra Volcano, Isabela Island, Galápagos Archipelago, *Geol. Soc. Am. Bull.*, *107*(12), 1398–1410, doi:10.1130/0016-7606(1995)107<1398:PVASDO>2.3.CO;2.

Rietbrock, A. (2001), P wave attenuation structure in the fault area of the 1995 Kobe earthquake, *J. Geophys. Res.*, *106*(B3), 4141–4154, doi:10.1029/2000JB900234.

Rychert, C. A., N. Harmon, and C. Ebinger (2014), Receiver function imaging of lithospheric structure and the onset of melting beneath the Galápagos Archipelago, *Earth Planet. Sci. Lett.*, *388*, 156–165, doi:10.1016/j.epsl.2013.11.027.

Sarker, G., and G. Abers (1998), Deep structures along the boundary of a collisional belt: Attenuation tomography of P and S waves in the Greater Caucasus, *Geophys. J. Int.*, *133*(2), 326–340, doi:10.1046/j.1365-246X.1998.00506.x.

Scherbaum, F. (1990), Combined inversion for the 3-dimensional Q-structure and source parameters using microearthquake spectra, *J. Geophys. Res.*, *95*(B8), 12,423–12,438, doi:10.1029/JB095iB08p12423.

Tepp, G., C. J. Ebinger, M. Ruiz, and M. Belachew (2014), Imaging rapidly deforming ocean island volcanoes in the western Galápagos archipelago, Ecuador, *J. Geophys. Res. Solid Earth*, *119*, 442–463, doi:10.1002/2013JB010227.

Villagomez, D. R., D. R. Toomey, E. E. Hooft, and S. C. Solomon (2007), Upper mantle structure beneath the Galápagos Archipelago from surface wave tomography, *J. Geophys. Res.*, *112*, B07303, doi:10.1029/2006JB004672.

Villagomez, D. R., D. R. Toomey, D. J. Geist, E. E. Hooft, and S. C. Solomon (2014), Mantle flow and multistage melting beneath the Galápagos hotspot revealed by seismic imaging, *Nat. Geosci.*, *7*(2), 151–156, doi:10.1038/NGEO2062.

Yun, S., P. Segall, and H. Zebker (2006), Constraints on magma chamber geometry at Sierra Negra Volcano, Galápagos Islands, based on InSAR observations, *J. Volcanol. Geotherm. Res.*, *150*(1–3), 232–243, doi:10.1016/j.jvolgeores.2005.07.009.